

Nonlinear analysis of masonry structures using fiber- section line elements

Matteo Peruch | Enrico Spacone | Guido Camata

Department of Engineering and Geology,
University G d'Annunzio of Chieti
Pescara, Chieti, Italy

Correspondence

Matteo Peruch, Department of
Engineering and Geology, University G.
d'Annunzio of Chieti Pescara, Chieti,
Italy.

Email: matteoperuch@gmail.com

Summary

For seismic analysis of unreinforced masonry (URM) buildings characterized by a box-like behavior, a widely accepted model is based on the equivalent frame idealization of walls. The equivalent frame model uses 1D elements to represent the vertical piers and horizontal spandrels which are connected by rigid nodes. The mechanical characterization of the elements is one of the crucial aspects to predict reasonably the building seismic behavior. Through the comparison with pseudo-static and dynamic experimental tests performed on two-story full-scale buildings, this paper validates the frame modeling in the OpenSees framework, which includes a fiber-section force-based beam element for the axial-flexural behavior, coupled with a cyclic shear-deformation phenomenological law.

KEYWORDS

dynamic analysis, equivalent frame, pushover analysis, unreinforced masonry

1 | INTRODUCTION

Observed damage caused by earthquakes in the past has clearly shown that unreinforced masonry (URM) buildings are highly vulnerable (Sorrentino et al,¹ Zucconi et al²). If the piers are not properly

connected to the diaphragms to avoid pier out-of-plane overturning and to guarantee a box-like behavior, the seismic behavior is dominated by out-of-plane collapse mechanisms, rather than in-plane collapse mechanisms, and simple models based on linear and nonlinear kinematic approaches can be used to design effective retrofitting systems to avoid out-of-plane collapse. The vulnerability is higher when the buildings are made of masonry with poor mechanical characteristics, for example irregular stones or weak mortar, which can be frequently found in old buildings of historical centers. When the box-like behavior is guaranteed, the numerical models can properly describe overall seismic behavior of buildings. The seismic response can be calculated with 2D and 3D sophisticated finite element (FE) models which consider the mechanical and geometric characteristic of the entire building. However, this approach is generally suitable for simple structures because of the modeling complexity, the difficulty in calibrating the required mechanical parameters, and the high computational cost. The presence of a large number of old masonry buildings in seismic areas has motivated an increasing effort to develop reliable simple models, which can be used by professionals, to simulate the masonry in-plane behavior. In a widely accepted simplified approach (Magenes, ³ Magenes et al⁴), the masonry structural elements are modeled with one-dimensional macroelements assuming an equivalent frame behavior and using conventional methods of structural mechanics to evaluate demand and capacity. A recent overview on different models for frame-type and macroelement modeling can be found in Marques and Lourenço. ⁵ This idea, initially developed in the 1970s (POR method,

Tomažević⁶), was further investigated by several researchers and implemented in software codes now widely used (eg, TREMURI Lagomarsino et al,⁷ SAM Magenes and Della Fontana⁸ and AEDES,⁹ in Italy). However, due to the modeling assumptions, the macroelements are not able to correctly simulate the reduced stiffness after cracking, and due to the simplified representation of the interaction M-N and V-N, the use of beam-type macroelements has some limitations. To overcome these limitations, Penna et al¹⁰ proposed a two-node macroelement which takes into account the coupling of axial and flexural response as well as the interaction of shear and flexural damage while modified two-dimensional macroelements have been recently proposed by Vanin and Foraboschi¹¹ using strut and tie models and by Calì et al¹² using nonlinear springs, the latter implemented in the computer code 3DMacro.¹³

Within the framework of the equivalent frame method, this paper presents the use of a fiber-section Timoshenko frame-element originally developed for reinforced concrete structures (Marini and Spacone¹⁴) and recently extended to URM walls (Raka et al¹⁵), for the nonlinear static and dynamic analysis of masonry structures. The analyses are carried out with the open source computational platform OpenSees (Mazzoni et al¹⁶).

2 | THE FORCE - BASED EQUIVALENT FRAME MODEL

In the equivalent frame model (EFM), the wall deformation is assumed to be lumped in piers and spandrels that are modeled using the “frame” macroelement, while the intersection zones (nodes) are considered rigid and are modeled using “rigid link” elements (Figure 1). The macroelement used in the present

work is composed of a force-based beam element (FBE) coupled with a phenomenological law that describes the shear behavior (Figure 2).

The fiber-section discretization allows for a relatively accurate description of the axial-flexural behavior, while the force-based formulation, ensuring equilibrium between bending moment and shear force, guarantees a perfect coupling between the beam element and the phenomenological shear law.

In the FBE formulation, material behavior is modeled by well-established uniaxial constitutive laws. The “Kent-Scott-Park with linear tension softening” material uniaxial constitutive law (Kent and Park,¹⁷ Scott et al,¹⁸ Mander et al¹⁹)

is used to simulate the behavior of masonry and concrete fibers, “Concrete02” command in OpenSees.

Modeling elements with negligible tensile strength, as in the case of URM elements, leads to inevitable convergence problems. To stabilize the numerical solution, elastic fibers with small area are added to the fiber cross sections. These fibers stabilize the numerical solution by keeping the section stiffness matrix nonsingular without influencing significantly the element overall response. The “elastic” material uniaxial constitutive law is used to simulate the stabilizing fibers behavior (OpenSees “Elastic” command).

The selection of the phenomenological shear law and the calibration of its mechanical parameters is central to describe accurately the wall behavior. Starting from the total response of a wall element (determined experimentally or analytically), the shear response is defined by subtracting the axial-flexural component (which corresponds to the FBE's response) from the total response.

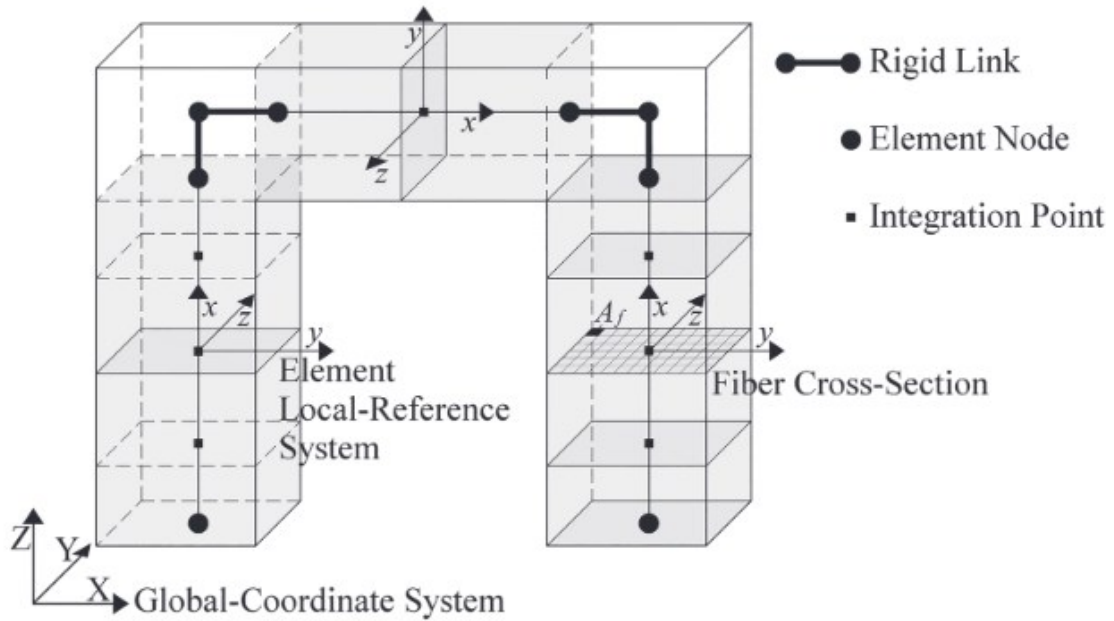


FIGURE 1 Equivalent frame discretization

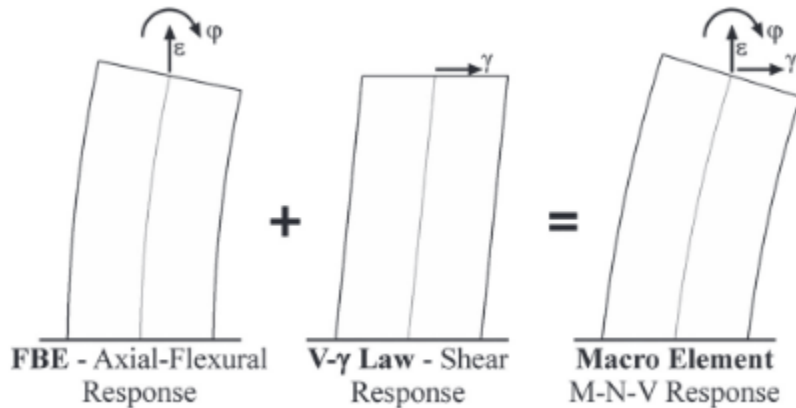


FIGURE 2 Macroelement

As reported in FEMA 273, ²⁰ the main failure mechanisms for a masonry panel pushed by horizontal loads are

(Figure 3) (a) rocking, horizontal cracks that open due to tensile stresses; (b) flexural failure, crushing of compressed toe; (c) shear failure, step crack in mortar joints; (d) shear failure, inclined diagonal cracks that open due to excessive tensile stresses; and (e) shear-sliding failure, sliding after the formation of a horizontal crack on a bed-joint. The in-plane failure of masonry walls is often a combination of these modes.

The proposed macroelement reproduces the axial-flexural failure mechanism with FBEs and the shear failure with phenomenological laws. Failure occurs through the mechanism that has the lowest capacity. Rocking and shear-sliding failure are not considered in this study.

The trilinear “hysteretic” material uniaxial constitutive law is used to simulate the shear behavior of the cross sections (OpenSees “Hysteretic” command). The constitutive law considers force and deformation pinching, damage due to ductility and energy, and degraded unloading stiffness. The response envelope, in both positive and negative loading directions, is defined by three significant points (expressed in terms of “shear force-shear strain”) as shown in Figure 4.

Point $V'-\gamma'$ corresponds to the end of the elastic phase of the shear response, point $V_n-\gamma_n$ is the shear response peak, and point $V_u-\gamma_u$ represents the ultimate shear response. A constant residual shear strength is assumed for shear strain larger than γ_u .

The determination of the shear strength V_n is fundamental for the calibration of the shear behavior law. For URM wall elements, a good estimation of V_n is given by Turnšek equation (Turnšek and Čačovič²¹):

$$V_n = \frac{f_{m,t} \cdot l \cdot t}{b} \sqrt{1 + \frac{\sigma_0}{f_{m,t}}} \quad (1)$$

where $f_{m,t}$ is the masonry diagonal tensile strength, σ_0 is the section average compression stress ($\sigma_0 = N/(l \cdot t)$), l and t the width and the thickness of the wall section, respectively, and b a parameter that depends on the pier aspect ratio h/l (h height of the wall) and ranges between 1.0 and 1.5 ($b = 1.0$ for $h/l \leq 1$; $b = h/l$ for $1.0 < h/l < 1.5$; $b = 1.5$ for $h/l \geq 1.5$).

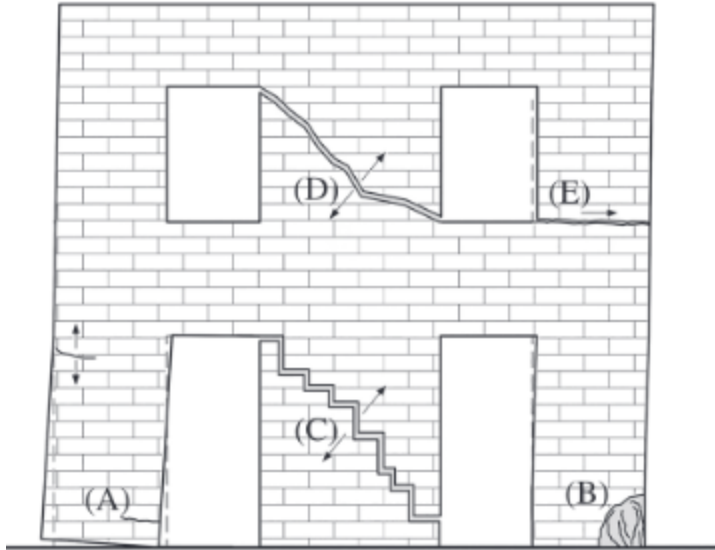


FIGURE 3 URM structure in-plane failure mechanisms

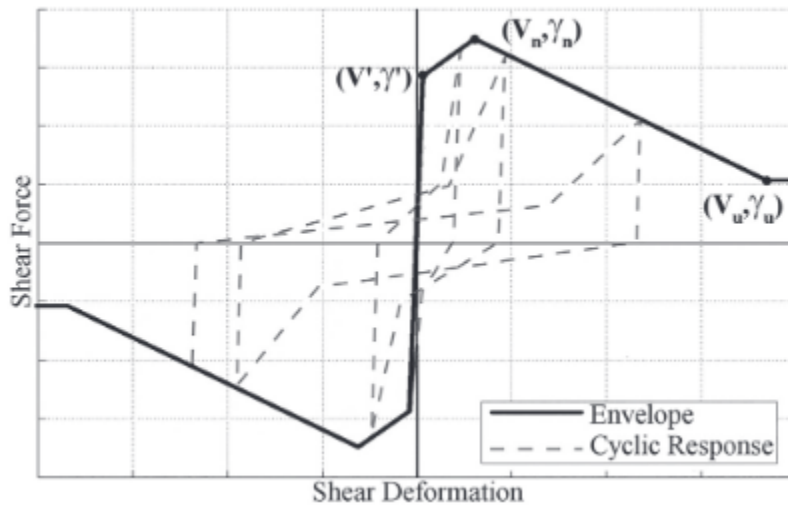


FIGURE 4 Shear behavior law

From the analysis of the experimental data collected for URM panels (Magenes and Calvi, 22 Manzuori et al,23

Anthoine et al24), V' can be assumed equal to the 60% of V_n , while the corresponding shear strain γ' is equal to the shear strain of an elastic Timoshenko cantilever beam:

$$\gamma' = c_s \cdot \frac{k \cdot V'}{A \cdot G_m} \quad (2)$$

where c_s is a correction coefficient (assumed equal to 2.0 in the analyses), k is the shear coefficient (1.2 for rectangular cross sections), A is the total cross-section area, and G_m is the masonry shear modulus. The remaining points of the response envelope are calibrated to obtain a good correspondence with the experimental data in terms of total response envelope, cyclic strength and stiffness degradation, and dissipated energy. In the following sections, the average calibration values for the analyzed URM structures will be provided.

It is important to note that the shear behavior law considered in this study does not depend on axial load N , so once set the shear law parameters remain constant during the analysis. It is clear that for elements with constant axial load this does not constitute a problem, but in real structures during the seismic event axial loads acting on the elements vary influencing the shear strength V_n (see Equation 1). Generally, in the spandrels, the value of N is almost null in static conditions, but under seismic loads it can vary considerably, leading to shear failure. The variation of N is difficult to predict as it depends on numerous factors such as the spandrel type and the interaction with the piers which affects the constraint conditions. Considering this difficulty, making a conservative choice, the shear strength of spandrels is calculated with Equation 1 considering homogeneous cross section and σ_0 equal to 0. It is important to note that spandrels might have composite cross sections due to the presence of slab and lintel, so it will be necessary to refer to ad hoc formulas for calculating the shear strength.

In the piers, the dynamic action caused by earthquakes induces a variation of N in a range around the initial value

$N_{Gravity}$ due to the gravity loads. Therefore, a method is needed to define the $V_{n,Analysis}$ value (shear strength value used in the analysis) in order to reduce the consequences caused by this shear law limitation. For each pier, the “theoretical strength domain” is determined as the minimum between the flexural capacity V_{flex} computed through a sectional analysis (eg, moment-curvature analysis) and the shear capacity V_n computed with Equation 1. For the calculation of the flexural capacity V_{flex} , the wall elements are considered fixed at both ends. This approximation result in a shear span equal to half the height of the element. The strength domain is expressed as a function of the axial force N . As shown in Figure 5, the strength domain is divided into two fields: “flexural failure” field and “shear failure” field. Axial force value N_{Limit} represents the boundary between the two fields. For piers that present flexural failure mechanism, with $N_{Gravity}$ (axial force due to gravity loads) less than N_{Limit} , $V_{n,Analysis}$ will be set equal to the shear capacity value at the intersection between the flexural capacity domain and the shear capacity domain determining an “analysis strength domain” that preserves the relationship between axial force and failure mechanism allowing to correctly determine the failure mechanism but underestimating the shear capacity in the shear failure field, as shown in Figure 5A. For piers that present shear failure mechanism, with $N_{Gravity}$ greater than N_{Limit} , $V_{n,Analysis}$ will be set equal to the shear capacity value corresponding to the gravity loads condition determining an “analysis strength domain” that does not preserve the relationship between axial force and failure mechanism within the range $[N_{Limit} - N_{Gravity}]$ leading to erro-

neous evaluation of the failure mechanism and an overestimation of the shear capacity, as shown in Figure 5B. Despite this incongruity, considering that the shear strength V_n has almost linear dependence on axial load N with a $\Delta V_n/\Delta N$ ratio lower than 20%, the “analysis strength domain” appears to be a good approximation of the theoretical one. In both cases, it is necessary to check if during the analysis the variation interval of the axial force and the assigned $V_{n,Analysis}$ value are compatible.

Many experiments have been conducted to investigate the in-plane properties of URM piers, and quasi-static tests are typically performed under a given constant axial load by applying a monotonic or cyclic lateral force. Tests conducted in this manner provide data on damage progression, ultimate strength, and drift ratio response of the element (Magenes and Calvi,²² Manzuori et al,²³ Anthoine et al²⁴). To validate the frame equivalent model, it is necessary to analyze more realistic masonry walls.

Section 3 presents the numerical results of pushover analyses of two different walls of the two-story URM building tested by Magenes et al²⁵ (Calvi et al²⁶). While, Section 4 presents the results of a dynamic analysis of a full-scale two-story building tested by Magenes et al²⁷ (Senaldi et al,²⁸ Senaldi ²⁹).

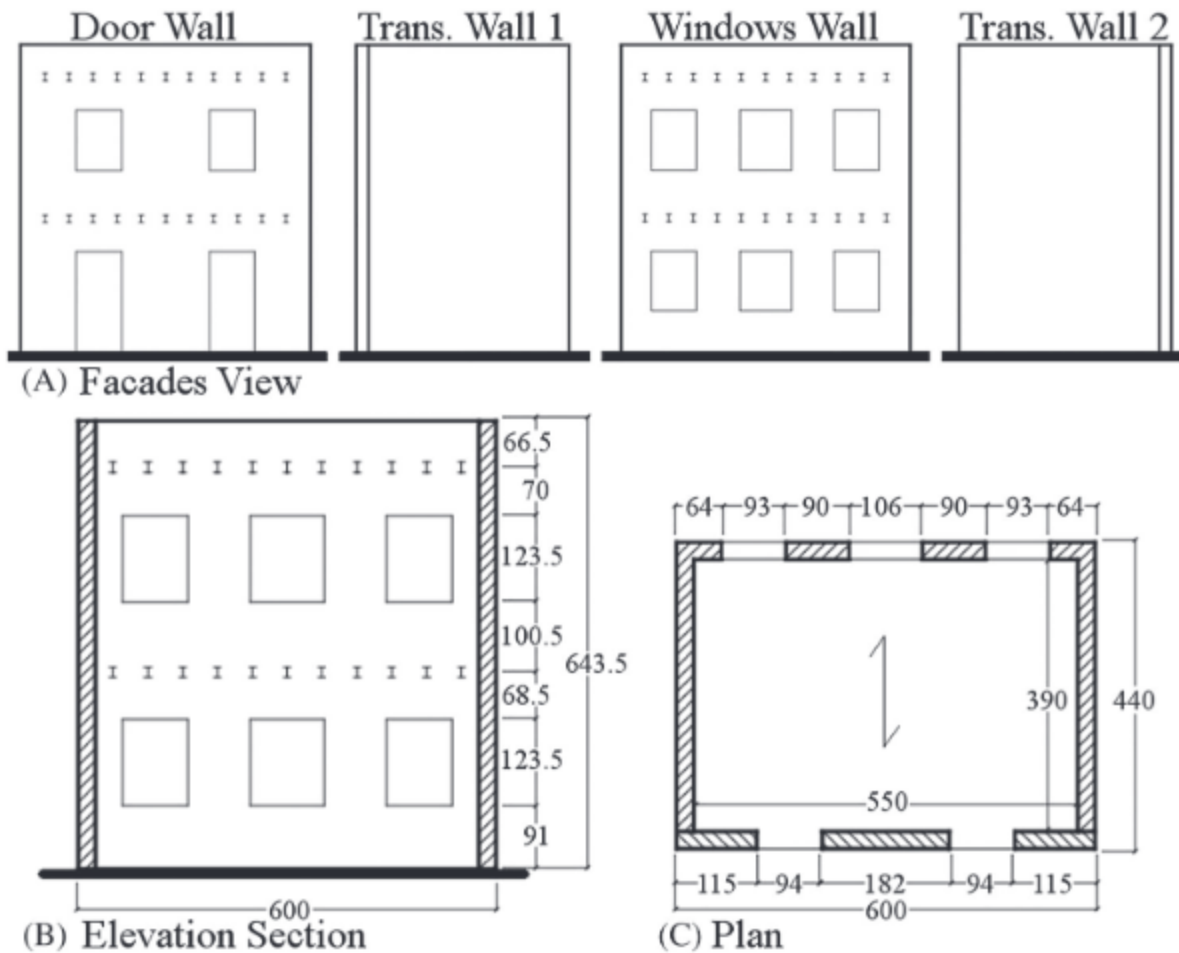


FIGURE 6 Tested structure (units in centimeters)

3 | NONLINEAR PUSH OVER ANALYSIS OF FULL-SCALE TWO-STORY URM WALLS

The first case study is a quasi-static test conducted at the University of Pavia by Magenes et al²⁵ of a full-scale two-story URM building. The results from quasi-static experimental test are compared with the results of cyclic and monotonic nonlinear pushover analysis obtained with an equivalent frame idealization. Figure 6 shows the views of the four façades of the building; “Door” and “Windows” walls were oriented along the pushing direction.

The two-story structure with plan dimensions of 6.00×4.40 m and height of 6.44 m circa, as shown in Figure 6, is made of unreinforced solid fired-clay bricks masonry with a nominal thickness of 25 cm and a self-weight of 1835 kg/m^3 .

The floors are made of a series of isolated steel beams (I section, 140-mm depth) and are supported by the Door and Windows walls, Figure 6B-C. The floors are loaded with concrete blocks for a total of 248.4 kN at the first floor and 236.8 kN at the second floor. The test was carried out by applying cyclic displacements of increasing amplitude at floor levels by means of four displacement-controlled screw jacks. The structure is composed of two different parts because of the flexibility of the floor diaphragms and because of the presence of separation joints between the Door wall and the Transversal walls (Figure 6C). For this reason, the Door wall can be analyzed independently from the rest of the structure.

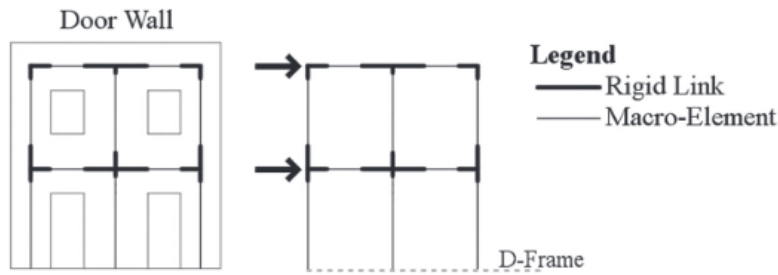
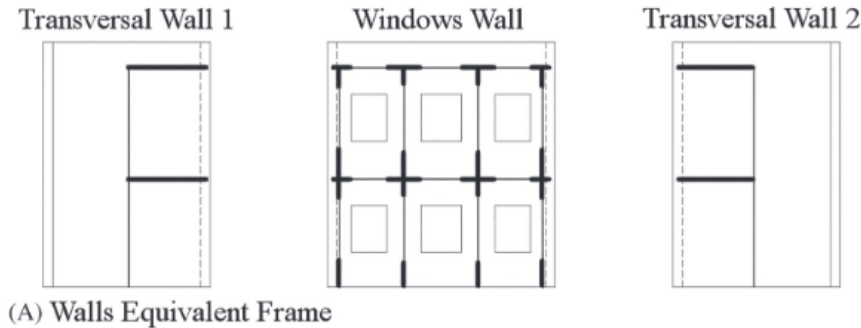
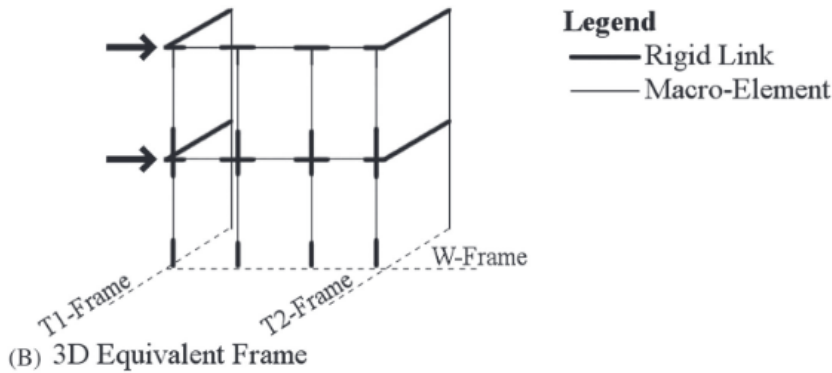


FIGURE 7 Door wall equivalent frame model



(A) Walls Equivalent Frame



(B) 3D Equivalent Frame

FIGURE 8 Windows wall equivalent frame model

3.1 | Equivalent frame models

The EFM's are shown in Figures 7 and 8. The Door wall is modeled as a 2D EFM, while the Windows wall is modeled as a 3D EFM due to connection with the Transversal walls. An “equal degrees of freedom constraint” at story levels (for the horizontal displacements) is imposed to the nodes of the Door and Windows walls. For both EFM's, piers height and spandrels length are determined following the method proposed by Dolce.³⁰ The self-weight of the elements is applied as distributed load as well as the vertical load transmitted by the floors.

All piers and spandrels have a rectangular cross section. All the cross sections of the elements are discretized in two principal directions. At the corners of the cross sections, additional elastic fibers with elastic modulus of 1000 MPa and cross-section area of 20 mm² have been inserted to stabilize the numerical solution.

Table 1 shows the main mechanical characteristics (obtained from test on masonry prisms) assigned to the fibers used to discretize the masonry: compressive strength f_m ; diagonal tensile strength $f_{m,t}$; modulus of elasticity E_m ; and shear modulus G_m . The ultimate compressive strength $f_{m,u}$ is assumed equal to 10% of the f_m , while the ultimate strain ϵ_u is assigned so as to compensate the plastic localization (considering a FBE with four integration points, $\epsilon_u \approx 2\%$)

according to the approach proposed by Coleman and Spacone.³¹

From Magenes et al.²⁵ and Binda et al.³²

To define the shear behavior law, the first stiffness degradation shear strength V' and the ultimate shear strength V_u are expressed as a percentage of maximum shear strength V_n . Table 2 shows the shear law average envelope parameters obtained by interpolation of experimental data deriving from experimental tests on masonry walls.

V' , γ_n , V_u , and γ_u average values determined from Magenes and Calvi,²²

Manzuori et al.,²³ and Anthoine et al.²⁴

3.2 | Test sequence and analysis parameters

During the experimental test, the structure is subjected to a series of cycles with increasing target displacement. Figure 9 shows the complete displacement sequence at the second floor. Analyzing the data related to the forces generated by the actuators, we can assume a ratio of 1:1 between the force applied to the first floor and that applied to the second floor.

The results in terms of displacements, total base shear strength V_{base} , and failure mechanisms of a quasi-static cyclic analysis are compared with the experimental ones. In addition, a pushover analysis with target displacement of 23 mm

TABLE 1 Masonry mechanical characteristics

f_m , MPa	$f_{m,0}$, Mpa	E_m , Mpa	G_m , Mpa
6.2	0.18	1490	480

TABLE 2 Shear behavior law envelope parameters

V'	γ'	V_n	γ_n	V_u	γ_u
$0.6*V_n$	Equation 2	$V_{n,Analysis}$ (Equation 1)	0.0015	$0.5*V_n$	0.01

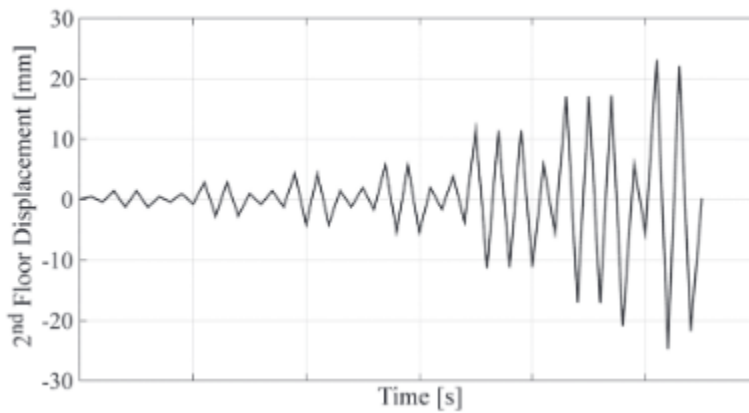


FIGURE 9 Second floor displacement sequence

(that corresponds to the maximum test target displacement) is performed to evaluate the monotonic response of the EFMs. The nonlinear cyclic and monotonic static analysis are performed using a Newton-Raphson solution algorithm combined with a displacement control integration method using as control node the top floor node where the force is applied (as shown in Figures 7 and 8). The convergence of the analysis is controlled by means of an energy convergence test (10^{-3} tolerance).

(that corresponds to the maximum test target displacement) is performed to evaluate the monotonic response of the EFMs. The nonlinear cyclic and monotonic static analysis are performed using a Newton-Raphson solution algorithm combined with a displacement control integration method using as control node the top floor

node where the force is applied (as shown in Figures 7 and 8). The convergence of the analysis is controlled by means of an energy convergence test (10^{-3} tolerance).

3.3 | Experimental damage

Figure 10 shows the damage status detected at the end of the experimental test for the Door and Windows walls. In both

walls, the damage is concentrated in the base piers and in the first floor spandrels. The second floor lateral piers of Door

wall develop rocking mechanism as shown by the horizontal cracks at the end of the piers, while the central pier does

not present the formation of any cracks. The second floor piers of Windows wall do not crack; therefore, the response is

elastic. In both walls, the spandrels of the second floor are cracked horizontally.

The base left piers of the Door wall fails in shear in pulling direction while in pushing direction develops rocking

mechanism due to the reduction of the axial load. The base right pier presents the same failure mechanisms as the base

left pier but in opposite directions. The base central pier fails in shear in both directions. According to the crack pattern,

the first floor spandrels fail in shear.

The base lateral piers of the Windows wall develop rocking mechanism, while the base central piers fail in shear.

According to the crack pattern the first floor lateral spandrels fail in shear.

3.4 | Analysis results

The nonlinear cyclic and monotonic static analysis results are shown in the following paragraph. The results in terms of

displacement, base shear, and failure mechanism are compared with the experimental data.

3.4.1 | Door wall results

Figure 11A-B show the results of the cyclic analysis of Door wall. The comparison with the experimental data shows a

good match in terms of floors displacement and base shear. The numerical response is slightly stiffer in the initial part

but follows with sufficient approximation the peak response and the softening phase. The EFM slightly overestimates

the base shear, 160 kN versus an experimental base shear of 150 kN (+ 6.7%). This difference is due to the simplifica-

tions introduced in the modeling: the shear behavior law limitations; the interaction between piers and spandrels that

affects the constraint conditions of the elements; and the inability of the FBE to correctly simulate the loss of strength

and stiffness due to the formation of rocking mechanism favored by the axial load reduction

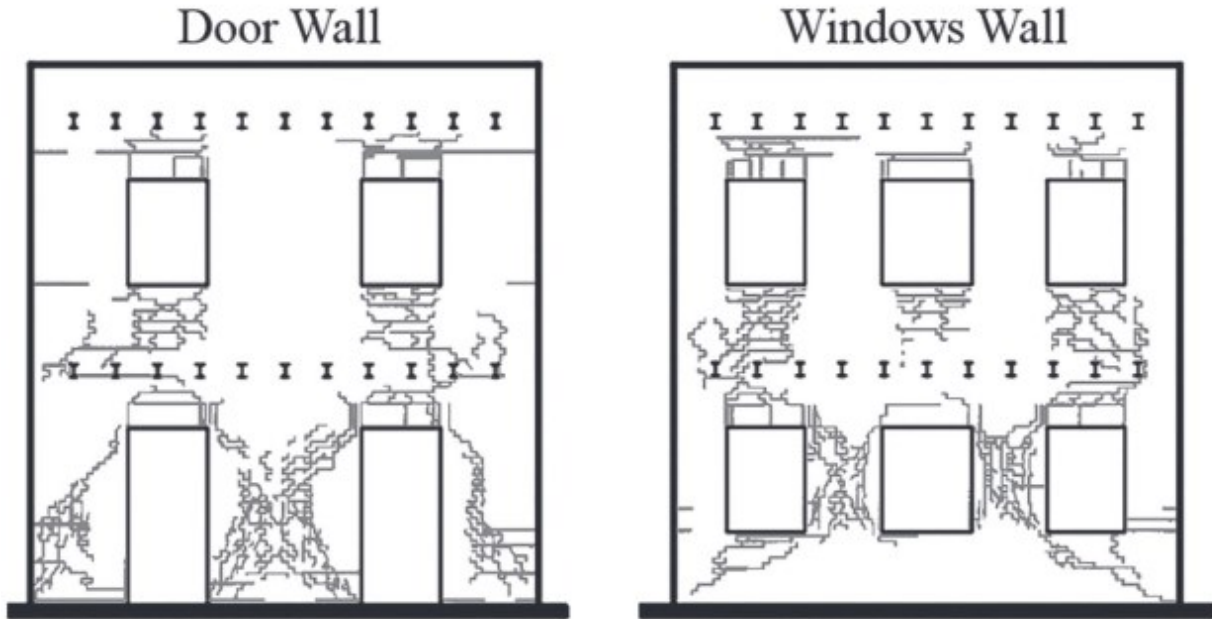


FIGURE 10 Damage at the end of the test (adapted from Magenes et al25)

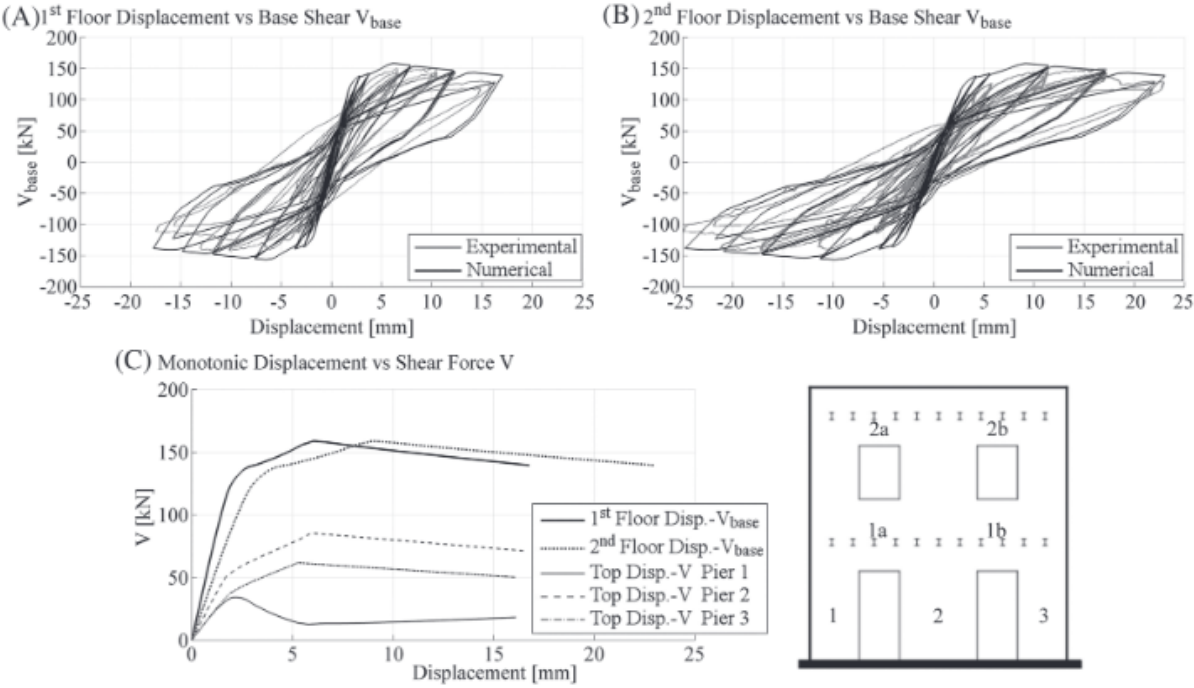


FIGURE 11 Door wall cyclic and monotonic analysis result
 Figure 11C shows the results of the monotonic analysis of Door wall. The first and second floor versus base shear curves represent the cyclic response envelopes. Pier 1 fails in flexure; the maximum load is 34 kN for a drift ratio of

0.09%. The low resistance value and the early start of the softening phase are determined by the reduction of the axial load and by the low tensile strength of the element. Pier 2 fails in shear. The maximum shear capacity is 85 kN, corresponding to a displacement at the top of 5.9 mm (0.22% drift ratio) completing the development of the shear failure mechanism reaching a maximum displacement of 16.5 mm (0.62% drift ratio). Also, pier 3 after reaching the maximum shear strength of 62 kN at 5.3-mm top displacement (0.21% drift ratio) fails in shear. The second floor piers fail in flexure. The first floor spandrel 1a reaches 36 kN, while spandrel 1b fails in shear with a maximum shear strength of 65 kN.

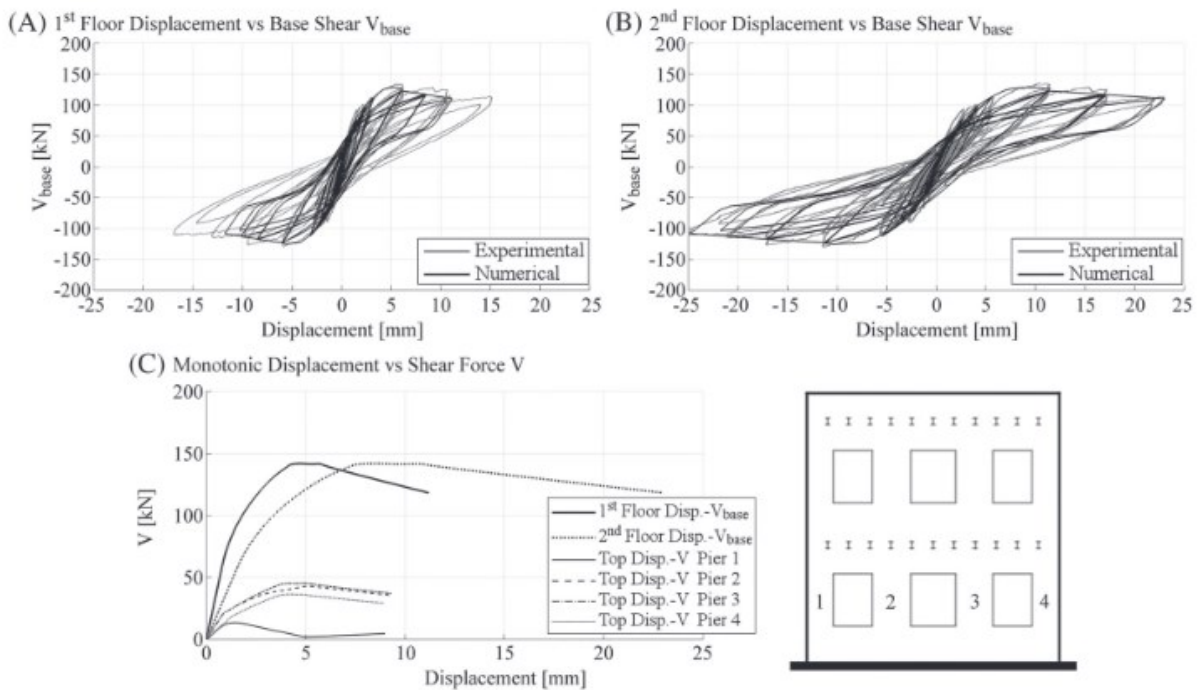


FIGURE 12 Windows wall cyclic and monotonic analysis results

At the second floor, the spandrels response is similar to the first floor spandrel with a maximum shear strength equal to

22 kN for spandrel 2a and 52 kN for spandrel 2b.

For the Door wall, cyclic and monotonic analyses provide consistent results in terms of elements response. The cyclic

analysis mirrors the response of the monotonic analysis according to the loads direction.

3.4.2 | Windows wall results

Figure 12A-B shows the results of the cyclic analysis of Windows wall. Figure 12B shows a good match between exper-

imental and numerical overall response in terms of initial stiffness, response peak, base shear, and displacement. Figure

12A shows that the first floor maximum numerical displacement is equal to 10 mm versus the experimental one equal to

15 mm. The numerical results show a linear deformation trend (along the height of the structure), while the experimen-

tal test shows that about 70% of the deformation is concentrated on the first floor, due to the formation of a soft story

mechanism. Despite this difference, attributable to the equivalent frame modeling and to the macroelement limits, the

failure mechanisms of the various elements are compatible with the experimental results.

Figure 12C shows the results of the monotonic analysis of Windows wall. Pier 1 after the peak strength of 13 kN

softens, and at 0.31% drift ratio the shear resistance is very low. Pier 2 reaches the maximum strength at 43 kN for a

top displacement of 5.1 mm (0.29% drift ratio) and then softens failing in flexure. Pier 3 reaches the peak strength at

45 kN at 5.1-mm top displacement (0.29% drift ratio); the pier fails in shear at 9.3 mm (0.52% drift ratio). In the case

of cyclic analysis, piers 2 and 3 fail in shear in both directions, correctly reproducing the experimental result. The alter-

nating variation of axial load on piers 2 and 3 causes the increase of the flexural strength whose value exceeds that of the

shear strength V_n (preset at the beginning of the analysis) inducing the development of shear failure mechanism. Pier 4

reaches a peak flexural strength of 36 kN at 0.26% drift ratio. The second floor piers fail in flexure. All the first floor spandrels fail in shear with maximum shear force of 53 kN, while the second floor spandrels fail in flexure.

For the Windows wall, the structural response evolution due to cyclic loading determines a different failure mechanism for pier 2. Despite this difference, cyclic and monotonic analyses provide consistent results.

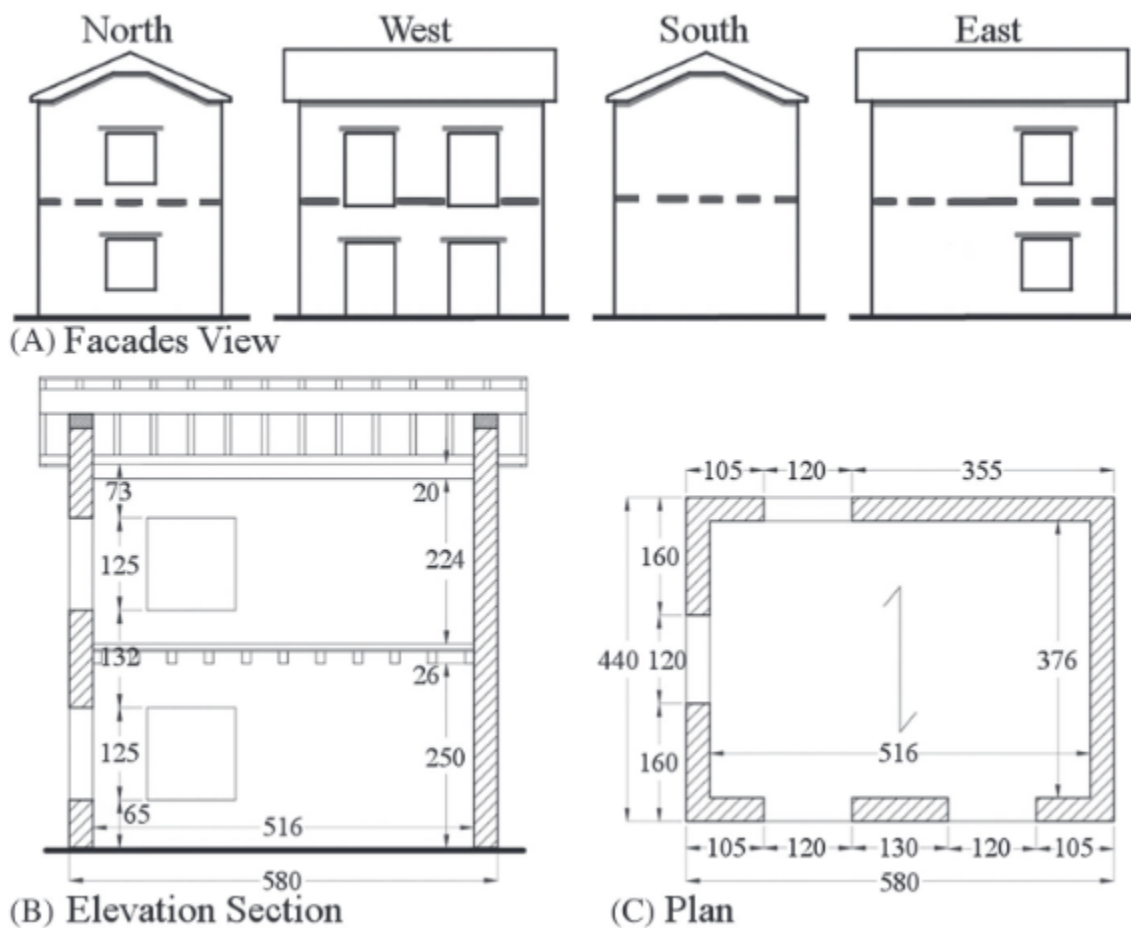


FIGURE 13 Building prototype 3 (units in centimeters)

4 | N O N L I N E A R T I M E - H I S T O R Y A N A L Y S I S O F F U L L - S C A L E T W O - S T O R Y U R M B U I L D I N G

In 2010, an experimental campaign was carried out by Magenes et al²⁷ on

full-scale two-story building on the shaking table at the University of Pavia (EUCENTRE laboratory). Three different prototypes, intended to represent old stone masonry buildings, with different types of strengthening for the roof and floor were tested by the Authors: deformable wooden floor and deformable roof (building prototype 1); deformable wooden floor with steel ring beam and roof with reinforced masonry ring-beam (building prototype 2); and rigid floor and rigid roof (building prototype 3). Considering building prototype 3, the results from dynamic experimental tests (Senaldi²⁹) are compared with results of nonlinear time-history analysis obtained with a 3D model based on the equivalent frame idealization. Figure 13 shows the views of the four façades of the building; West and East walls were oriented along the shake table motion while North and South walls were perpendicular to it. The two-story structure is made of unreinforced double-leaf stone masonry with a nominal thickness of 32 cm, and the self-weight of the masonry is 2300 kg/m³. The intermediate floor is made of wooden beams (12 × 16 cm cross section), and a single layer of 3-cm-thick planks. The floor is supported by the East and West walls (Figure 13B-C). The floor diaphragm is stiffened by a 7-cm-thick reinforced concrete slab (steel welded mesh $\phi 8$ 15 × 15 cm) and connected to the wooden structure by steel studs ($\phi 14$). The connection between the floor and the walls is made of steel threaded bars ($\phi 14$ to 140-cm length) passing through the wall thickness and embedded in the concrete slab. The anchorage of the connecting bars is guaranteed with steel plates placed on the wall outer faces. The roof is connected to the walls with reinforced concrete rings (32 × 20 cm cross section—C25/30 Concrete—

B450 steel, 4 ϕ 16 longitudinal bars and ϕ 8@20-cm stirrups) which are at the top of the perimeter walls. The roof structure is made of a central ridge beam (20 × 32 cm cross section) and two lateral spread beams (32 × 12 cm cross section) arranged in the longitudinal direction. The roof is completed with purlins (8 × 12 cm cross section—50-cm spacing), and it is covered by a single 3-cm-thick plank layer. Three additional layers of spruce plywood panels (3 × 2.1-cm thickness) glued and doweled to the wood structure stiffen the roof. In addition, continuous steel plates (8 cm wide and 0.5 cm thick) are fixed all along the roof perimeter. The roof is completed by the addition of tiles.

4.1 | Equivalent frame model

The EFM of building prototype 3 is shown in Figure 14. Following the stiffening interventions of the floor and roof and their good connections to the walls, the floor diaphragms are considered rigid in their own plan. To simulate the effects of the rigid diaphragms in the EFM, an “equal degrees of freedom constraint” at story levels (for the transverse displacements) is imposed to the nodes. The piers height and the spandrels length are determined following the method proposed by Dolce.³⁰

All piers and spandrels have a rectangular cross section. The intermediate spandrels have a wooden lintel on the bottom, while the upper ones also include a top reinforced concrete beam. Spandrels have been modeled assuming a perfect contact between the different materials (masonry, wood, and reinforced concrete) at the section level. All the cross sections of the elements are discretized in two principal directions. At the corners of the cross sections, when there is no tensile-resistant element (such as wooden lintel or RC beam), stabilizing fibers

with elastic modulus of 1000 MPa and cross section of 20 mm² have been inserted.

Table 3 shows the main mechanical characteristics assigned to the masonry fibers. The compression and tensile strength values are obtained from experimental “compression” and “diagonal compression” tests, respectively, as described in detail in Magenes et al. ³³

The shear behavior law, values used in the analysis are calibrated with the experimental test data on simple cantilever unreinforced double-leaf stone masonry panels (Magenes et al ³⁴). Table 4 shows the shear law average envelope parameters.

4.2 | EFM calibration

Once the EFM is defined, to compute the elements shear strength V_n , and configure the shear behavior constitutive laws, a preliminary gravity load analysis is performed. The EFM was calibrated with the experimental measurements of the natural vibration periods of the structure. The modal modes of the EFM are determined by modal analysis.

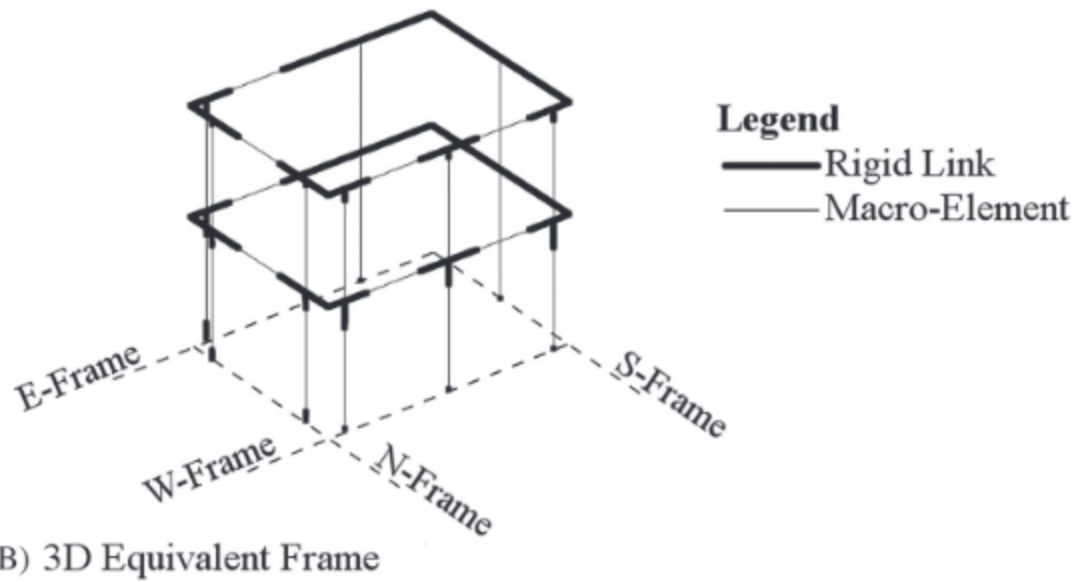


FIGURE 14 Equivalent frame model

TABLE 3 Masonry mechanical characteristics

f_m , MPa	$f_{m,t}$, MPa	E_m , MPa	G_m , MPa
3.28	0.14	2537	841

TABLE 4 Shear behavior law envelope parameters

V'	γ'	V_n	γ_n	V_u	γ_u
$0.6 \cdot V_n$	Equation 2	$V_{n,Analysis}$	0.005	$0.7 \cdot V_n$	0.01

Subsequently, through an iterative process, the modal modes are adjusted modifying the initial shear stiffness through the initial shear strain γ' parameter. The calibration is considered completed when the first numerical fundamental period is close to the experimental one of 0.136 seconds (7.35 Hz). This procedure improves the response of the EFM

in terms of initial stiffness and elastic response.

Table 5 reports the experimental and analytical fundamental initial periods and the predominant characteristics of the associated mode shapes (the experimental second mode data are not available). The comparison shows a good correspondence in terms of vibration periods.

Figure 15 shows the experimentally measured mode shapes, while Figure 16 shows the numerical ones. The discrepancy between the experimental and the analytical mode shapes is essentially due to the experimental method used for the modal identification (“random vibrations method,” Senaldi ²⁹) and to the approximation introduced in the numerical model (mainly, equivalent frame and rigid diaphragm assumptions).

The experimental mode shapes show a prevalence of deformation in the shaking direction and the presence of distortion in correspondence of the floor and the roof especially between the gutter level and the ridge beam.

The numerical first and fifth mode shapes present good correspondence with the experimental ones showing a predominant translational component in the shaking direction. The analytical second and fourth modes are translational.

TABLE 5 Experimental vs numerical modes

Mode	Experimental Modes		Numerical Modes			
	Period, s	Mode shape	Period, s	Mode shape	M_x , %	M_y , %
First	0.136	$DX - T$	0.135	$DX - T$	87.4	1.6
Second	-	-	0.134	$DY - T$	4.5	89.3
Third	0.071	$DX - T$	0.105	T	3.7	4.4
Fourth	0.059	$DX - T - D$	0.051	$DY_{\pm} - T$	0.0	4.5
Fifth	0.046	$DX_{\pm} - T - D$	0.049	$DX_{\pm} - T$	4.3	0.1
Sixth	0.038	$DX - T - D$	0.041	T_{\pm}	0.1	0.1

DX = translational mode shape in X direction (shaking direction).

DY = translational mode shape in Y direction (orthogonal to shaking direction).

T = torsional mode.

D = diaphragms distortion.

\pm = complex mode shape (floor and roof diaphragms move in opposite directions).

M_x = modal participation mass in X direction.

M_y = modal participation mass in Y direction.

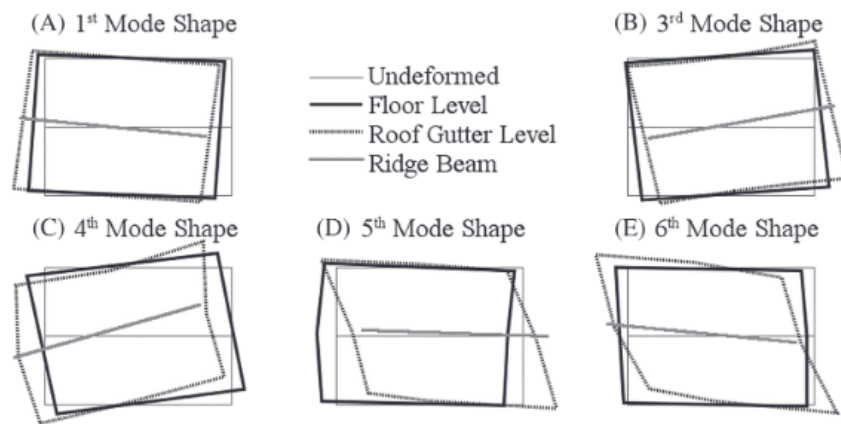


FIGURE 15 Top view of the experimental mode shape before dynamic tests (adapted from Senaldi 29)

(orthogonal direction compared with that of first and fifth modes), while third and sixth modes are torsional. The asymmetry of the structure results in a torsional component which influences all the modal shapes.

The results obtained can be considered consistent with the experimental data, and representative of the overall behavior of the structure. Furthermore, the response of the structure is dominated by the modes parallel to the orientation of the seismic input, and the two initial modes in this direction are fairly well represented by the EFM.

4.3 | Test sequence and analysis parameters

Table 6 shows the experimental test sequence of eight unidirectional dynamic excitations, from GM1 to GM8. All ground motions were derived by properly scaling the Montenegro record from Ulcinj-Hotel Albatros station of 15 April 1979 (Figure 17).

In the analysis, the acceleration measured at the base of the structure is used as seismic input. The actual PGA recorded at the base of the structure present higher values compared with the nominal PGA of the input signal, probably due to the interaction between the shaking table and the structure and the introduction of higher frequency components.

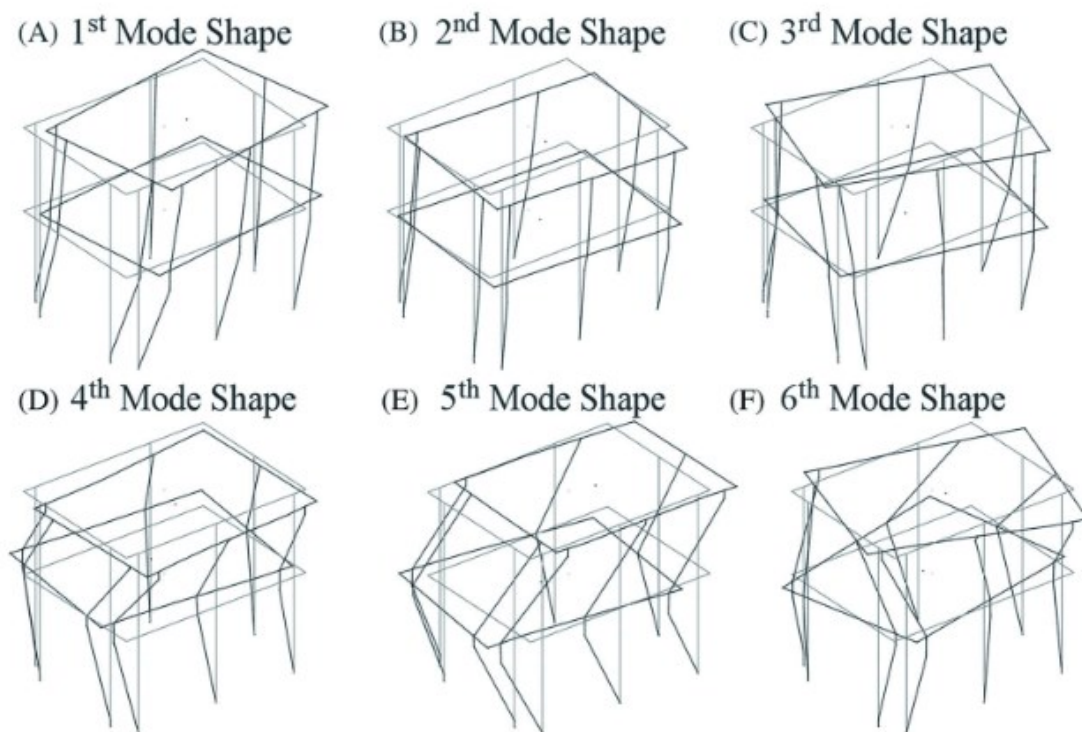


FIGURE 16 Eigenvalue analysis mode shapes before dynamic analysis

TABLE 6 Test sequence

TEST ID	Nominal PGA ^a , g	Actual PGA ^b , g
GM 1	0.05	0.12
GM 2	0.10	0.27
GM 3	0.20	0.55
GM 4	0.30	0.92
GM 5	0.40	1.28
GM 6	0.50	1.04
GM 7	0.60	1.49
GM 8—After shock	0.30	0.66

^aPGA of shaking table input signal.

^bPGA of shaking table output signal (feedback).

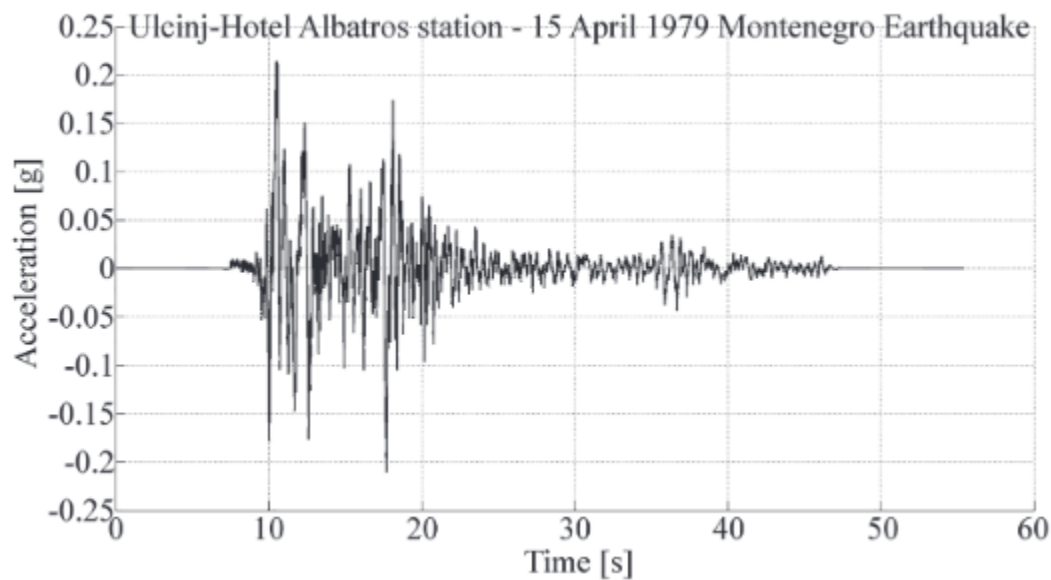


FIGURE 17 Reference ground motion

All the nonlinear time history analyses are performed in sequence, as reported in Table 6, using a Newton-Raphson solution algorithm combined with a Newmark integration method (average acceleration method $\alpha = 1/2$, $\beta = 1/4$) and Rayleigh damping proportional to the mass and the current stiffness matrix. The equivalent viscous damping ratio of 2% is the suggested values used in the dynamic analyses of the small-scale masonry structures model considered on this paper. The damping parameters are chosen to achieve an equivalent damping ratio of 2% at the first and fifth modal frequencies related to the two dominant modes (in terms of mode shape and

participation mass) in the shaking direction. The convergence of the analysis was controlled by means of an energy convergence test (10^{-3} tolerance).

4.4 | Analysis results

The time history analysis results are shown in the following paragraph. The results in terms of damage, fundamental periods, acceleration and displacement responses, maximum drift ratio, and base shear are compared with the relevant experimental data.

4.4.1 | Damage evolution

Figure 18 shows the evolution of damage during the test. The structure was built outside the laboratory and later moved and docked to the shaking table. During this operation, several cracks developed as shown in Figure 18A. Figure 18B,C shows the damage after medium and high intensity ground motions (in terms of PGA), respectively.

Damage is concentrated at the first floor piers of West and East walls. West and East walls, oriented in the shaking direction, guarantee almost all the resistance against the seismic action.

Damage in West and East walls is caused by in-plane mechanisms while the cracks on North and South walls are caused by out-of-plane mechanisms. The cracks at the ends of the spandrels begin to develop for low acceleration values; therefore, the spandrels behaved as trusses able to transfer only normal stresses. The ratio between shear demand V and shear capacity V_n is considered as damage indicator of the various elements. In Table 7, the ratio V/V_n is shown for the first floor piers of West and East walls (for piers IDs refer to Figure 18A).

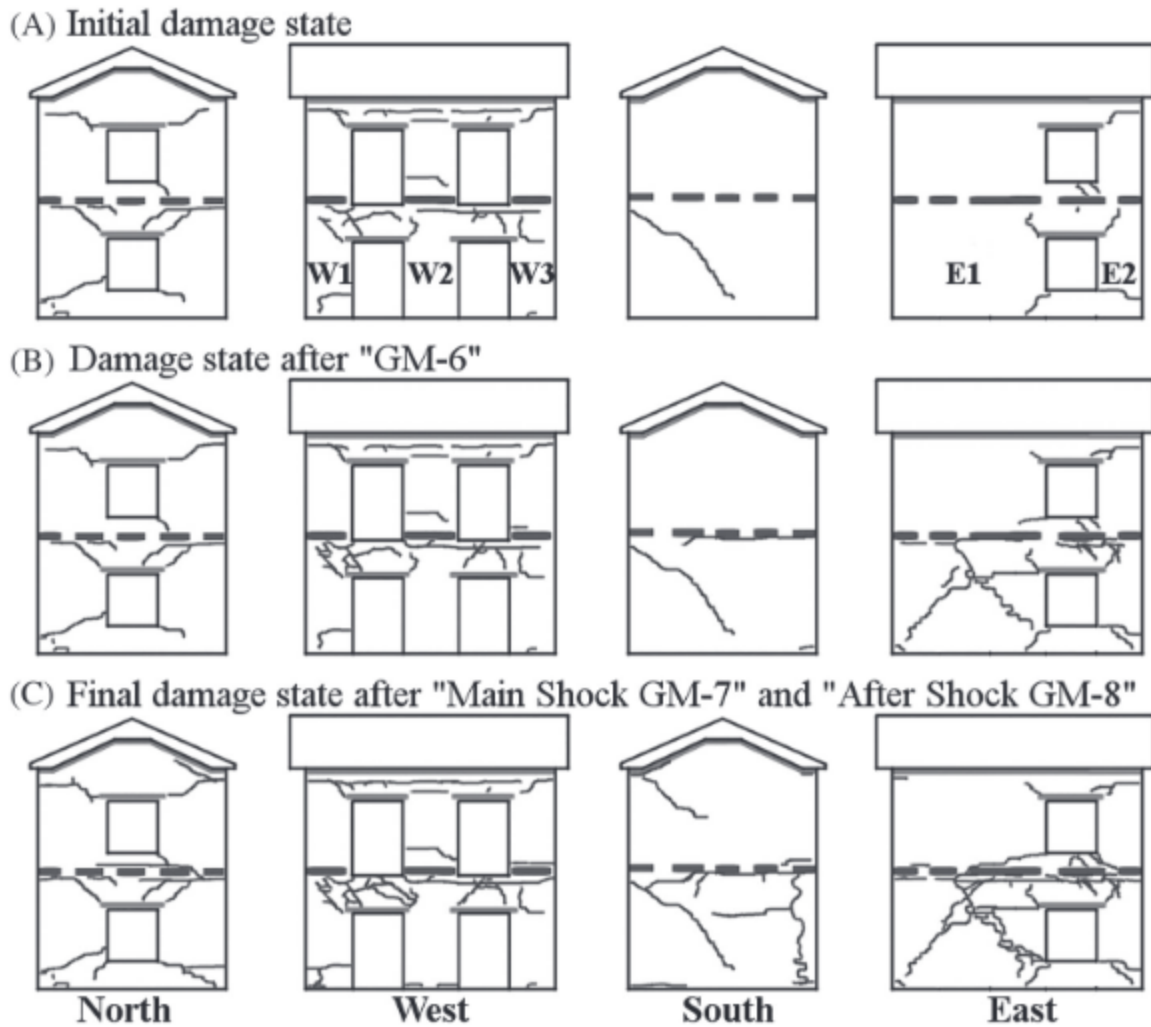


FIGURE 18 Damage evolution (adapted from Senaldi 29)

TABLE 7 Acting shear vs shear strength on West and East walls piers

Piers	V_n , kN	V/V_n , %						
		GM1	GM2	GM3	GM4	GM5	GM6	GM7
W1	67	7.8	12.6	24.3	40.4	46.4	55.1	68.5
W2	69	8.6	13.6	29.9	44.0	53.8	69.6	85.4
W3	67	9.7	15.6	35.3	53.2	66.2	86.0	98.5
E1	209	8.1	16.5	42.2	64.8	85.1	90.7	100.0
E2	57	9.4	13.4	26.6	37.1	49.4	47.8	60.9

As expected as the seismic intensity increases, the demand on the various piers increases. Up to GM4 test (actual PGA = 0.92 g), the damage is concentrated at the ends of the elements, horizontal cracks for the piers, and vertical

cracks for the spandrels. The average ratio V/V_n on the resistant piers is around 50%, while the floor drift ratio reaches the values of 0.165% for the East wall and 0.217% for the West wall. GM5 and GM6 are medium-high intensity ground motion with PGA values of 1.28 and 1.04 g, respectively. New horizontal and vertical cracks develop, and the cracks already opened continue to spread. During GM6, large diagonal cracks form on E1 pier, and the shear demand reaches 90.7% of its shear capacity for a 0.309% drift ratio. GM7 has a PGA of 1.49 g, and during this test piers E1 fails in shear reaching a maximum drift ratio of 0.372%. Slender Piers W1, W2, and W3 reach a maximum drift ratio of 0.503% with a response dominated by flexural behavior. During GM7 test, these piers show a rocking mechanism with consequent loss of strength and stiffness. The EFM cannot simulate the rocking mechanism; therefore, the slender piers maintain a flexural response. This results in greater shear forces and stiffer response. In the analysis, the most affected element by this model limitation is pier W3 which reaches a shear demand equal to 98.5% of its shear capacity. This shear force level indicates a developed shear mechanism close to failure, condition not detected experimentally.

4.4.2 | Fundamental mode periods

The damage evolution, and the resulting stiffness reduction, affects the behavior of the structure. To simulate correctly the nonlinear structural response induced by ground motions, the correspondence between the analytical and experimental fundamental vibration modes is deemed important. Table 8 reports the vibration period values calculated before each time-history analysis together with the experimental ones.

The EFM used in this study reproduces well the structural modes. In terms of

mode shapes, only the first and fifth modes (both parallel to the shaking direction and thus predominant in the structure response) are closely reproduced by EFM. A major source of difference between experimental and numerical mode shapes is the deformability of the floor slabs, which is not considered in the EFM. All modes show period increase, mainly due to the development of in-plane mechanisms on West and East walls, especially first and second in principal directions, confirming structural damage

TABLE 8 Fundamental mode periods evolution, experimental vs numerical

Ground Motion	First Period		Second Period		Third Period		Fourth Period		Fifth Period		Sixth Period	
	Exp	EFM	Exp	EFM	Exp	EFM	Exp	EFM	Exp	EFM	Exp	EFM
GM1	0.136	0.135	-	0.134	0.071	0.105	0.059	0.051	0.046	0.049	0.038	0.041
GM2	0.136	0.135	-	0.134	0.070	0.105	0.059	0.051	0.046	0.049	0.038	0.041
GM3	0.145	0.153	-	0.134	0.071	0.109	0.061	0.052	0.046	0.051	0.039	0.042
GM4	0.155	0.170	-	0.138	0.072	0.115	0.062	0.061	0.049	0.052	0.041	0.044
GM5	0.157	0.177	-	0.142	-	0.120	0.063	0.066	0.052	0.054	0.042	0.046
GM6	0.160	0.176	-	0.158	-	0.121	0.066	0.073	0.053	0.061	0.043	0.047
GM7	0.161	0.185	-	0.145	-	0.121	0.066	0.068	0.053	0.056	0.045	0.047
GM8	0.163	0.222	-	0.175	-	0.126	0.066	0.076	0.057	0.063	0.046	0.048

and the consequent loss of stiffness. Overall, the results obtained in terms of vibration periods are quite consistent with the experimental data and representative of the structural behavior.

4.4.3 | Acceleration and displacement response

The comparison between numerical and experimental results in terms of acceleration and displacement (evaluated at the top of West wall) is reported in Figure 19 for a time window of 11 seconds in order to compare a significant part of the responses.

Figure 19A,B shows the acceleration and displacement responses for GM1 and GM4 tests, respectively. The EFM reproduces well the experimental responses for ground motions of low and medium intensity in terms of PGA. The numerical acceleration and displacement responses show good agreement with

the experimental ones up to a nominal PGA of 0.3 g (actual PGA = 0.92 g referring to Table 6). Figure 19C shows the responses for test GM7 that represents the “main shock” with a nominal PGA of 0.6 g (actual PGA = 1.49 g referring to Table 6). The responses of the EFM for high intensity ground motion show a good correspondence in terms of acceleration but not in terms of displacements. The numerical response underestimates the experimental one especially in correspondence of the peaks. The discrepancy in terms of displacement is due to several phenomena not reproduced by the numerical model: rocking

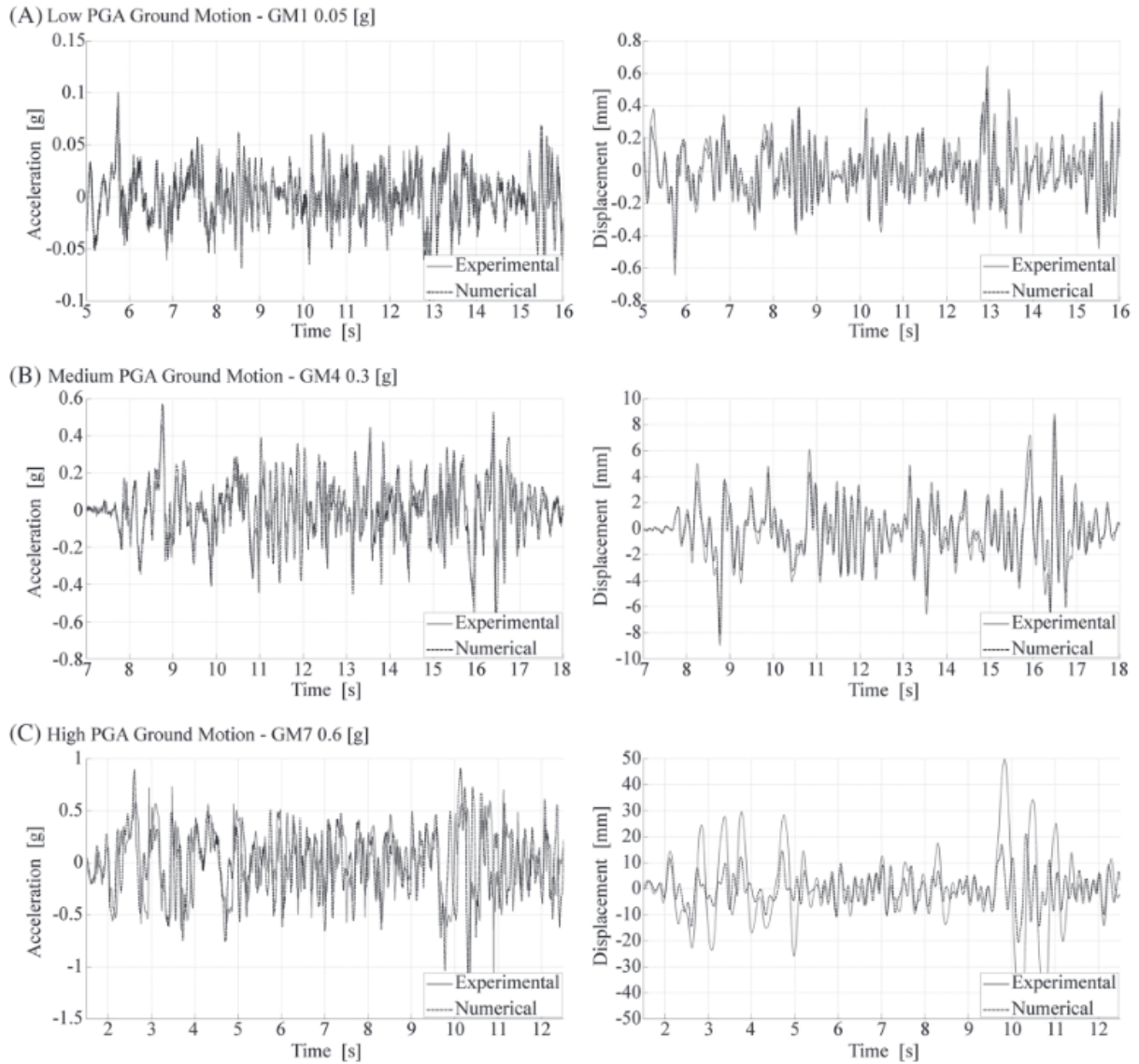


FIGURE 19 Top acceleration and top displacement responses for low, medium, and high PGA ground motion, experimental vs numerical

TABLE 9 Maximum drift ratio and base shear in positive and negative directions

Ground Motions	Experimental				Numerical			
	Drift, %		V_{base} , kN		Drift, %		V_{base} , kN	
	Pos.	Neg.	Pos.	Neg.	Pos.	Neg.	Pos.	Neg.
GM1	0.008	0.007	35	42	0.009	0.010	50	54
GM2	0.019	0.018	84	94	0.023	0.021	95	93
GM3	0.049	0.061	173	177	0.061	0.073	177	204
GM4	0.115	0.113	282	258	0.140	0.141	278	288
GM5	0.220	0.175	367	317	0.206	0.205	363	353
GM6	0.336	0.224	369	331	0.219	0.310	373	408
GM7	0.886	0.746	404	345	0.351	0.331	455	430
GM8	0.303	0.221	252	199	0.129	0.174	222	270

mechanism of slender piers of West wall not reproducible by EFM; rigid diaphragm hypothesis; piers-spandrels interaction; and shear behavior law calibration, especially with regard to the values of peak shear strength assigned to each

element 4.4.4 | Maximum drift ratio and base shear

Table 9 shows the maximum drift ratio at roof level and maximum base shear values achieved during each test. Data

show that the model predicts well the maximum drift ratio of the structure up to GM6 test. For GM7 and GM8 tests,

the predicted displacements are significantly lower than the experimental ones.

The reason for this discrepancy depends

on the damage propagation and the out-of-plane mechanisms of North and South walls that cannot be predicted cor-

rectly by EFM. Furthermore, the assumption of rigid diaphragms adopted in the EFM restrains the formation of local

deformations and when the piers are highly damaged, the selected 2% damping, which works well for low to moderate

damage, should be lowered when damage becomes large, because in this case almost all energy dissipation is due to

hysteresis.

In GM7 test after reaching the maximum base shear of 404 kN at 0.551% drift ratio, there is a loss of stiffness in the

West wall, due to pier rocking, resulting in a softening phase of the response

that leads to a drift ratio of 0.886% and a base shear of 282 kN. On the other hand, the numerical result shows a maximum shear of 455 kN at 0.351% drift ratio without the subsequent softening phase. The only element that loses strength is pier E1 that reaches the shear peak strength V_n and begins to soften (this result is compatible with the experimental cracking state of the element), while all other elements remain in the elasto-plastic phase without reaching the peak strength (the main damage at the end of the test is the horizontal crack at both end sections, Figure 18C). As mentioned earlier, the dynamic actions induce variations of the normal stress acting on the masonry piers. In slender piers, the reduction of axial load N promotes the formation of rocking mechanisms with loss of stiffness and shear strength. The EFM shear laws do not depend on the axial load N and thus cannot simulate the shear strength variation due to oscillations in the N values resulting in an overestimation of the base shear force especially in case of high accelerations.

5 | SUMMARY AND CONCLUSIONS

Through the comparison with pseudo-static and dynamic experimental tests performed by other Authors on full-scale URM two-story buildings, this work validates the proposed EFM in the OpenSees framework, which includes a fiber-section force-based approach for the flexural behavior, coupled with a cyclic shear-deformation phenomenological law.

Section 3 compares the numerical results of push-over analysis obtained with the proposed model for solid clay bricks walls of a two-story building tested through pseudo-static incremental loading, while Section 4 validates the numerical results of the proposed model for comparison with dynamic tests

performed on a two-story stone masonry building on the shaking table. It was shown that the proposed EFM simulates well the overall behavior of the simple structures studied. The condensation of the various nonlinear phenomena in the behavior of a macroelement (axial-flexure + shear) is acceptable.

To overcome the limitation of the shear behavior law, namely the nondependence on the axial load variation, a procedure based on the shear strength domain has been proposed for establishing the maximum shear strength to consider in the calibration process. The quality of the results may improve with more refined shear behavior laws which take into account the variation of axial load, and a more accurate modeling of the spandrel beams and their interaction with the pier elements. As shown in Bayer,³⁵ the resistant mechanisms of the spandrels are complex and depend on the characteristics of the spandrel, the constraint conditions, and the type of lintel. The proposed macroelement can only approximate the response of the spandrel by reducing it to the pure flexural and shear components. A better response could be obtained through the use of elements with concentrated plasticity; in this case, the difficulty would be the calibration of the phenomenological laws that govern the plastic hinges.

In the URM the absence of elements that resist traction makes the analyses more unstable numerically. The fiber sections need to be stabilized with additional elastic fibers which need to be calibrated to not influence significantly the overall stiffness and strength response of the macroelement, piers, and spandrels, in particular in time-history analysis. The use of nonlinear shear law causes convergence problems particularly in spandrel elements with large distributed loads.

In the analyzed cases, the interlocking effect between orthogonal walls may be

ineffective, for large displacements and high accelerations, resulting in a change of the structures static scheme. The use of rigid links to simulate the connection between the orthogonal walls limits the ability of the model to reproduce the evolution of this mechanism that significantly affects the overall response of the structures. Moreover, in slender piers, the axial load reduction triggers the formation of rocking mechanisms, which cannot be reproduced correctly with FBE. This limitation is compensated by the reduction in strength and stiffness, associated with the axial-flexural response, caused by the reduction of the axial load and the reduced tensile strength of the elements. For both structures considered in this paper, the numerical results obtained with the proposed model are satisfactory and show the capability of the analytical models to reproduce the response of the buildings in terms of forces, displacements, and failure mechanisms.

Despite the numerical instability issues and the limitations due to the shear behavior law, the simplicity and numerical efficiency make the proposed macroelement an effective tool for the analysis of URM structures within the framework of “equivalent frame method.”

ACKNOWLEDGEMENTS

The authors express a sincere gratitude to Prof. Magenes for giving the access to all the data of experimental tests done by the Eucentre at the University of Pavia, and they also like to thank Dr. Ilaria Senaldi, who provided the experimental test results that she elaborated during her PhD thesis, used in this paper to validate the numerical results of the proposed model. Partial financial support from the ReLUIS program of the Italian Civil Protection Agency is also acknowledged.

O R C I D

Matteo Peruch <https://orcid.org/0000-0001-6397-189X>

Enrico Spacone <https://orcid.org/0000-0002-8304-7028>

Guido Camata <https://orcid.org/0000-0003-4663-4140>

R E F E R E N C E S

1. Sorrentino L, Cattari S, da Porto F, Magenes G, Penna A. Seismic behaviour of ordinary masonry buildings during the 2016 Central Italy earthquakes. *Bull Earthquake Eng.* 2018. <https://doi.org/10.1007/s10518-018-0370-4>
2. Zucconi M, Ferlito R, Sorrentino L. Simplified survey form of unreinforced masonry buildings calibrated on data from the 2009 L'Aquila earthquake. *Bull Earthquake Eng.* 2018;16(7):2877-2911.
3. Magenes G. A method for pushover analysis in seismic assessment of masonry buildings. 12WCEE 2000: 12th World Conference on Earthquake Engineering, Auckland, New Zeland, Sunday 30 January-Friday 4 February, 2000; Paper 1866.
4. Magenes G, Della Fontana A. Simplified non-linear seismic analysis of masonry buildings. In: *Proceedings of the Fifth International Masonry Conference, London; 13–15th October, 1998; 8: 190–195.*
5. Marques R, Lourenço PB. Possibilities and comparison of structural component models for the seismic assessment of modern unreinforced masonry buildings. *Comput Struct.* 2011;89(21-22):2079-2091.
6. Tomaževič M. The Computer Program POR. Report ZRMK, Ljubljana, 1978 [in Slovenian].
7. Lagomarsino S, Penna A, Galasco A, Cattari S. TREMURI program: an equivalent frame model for the nonlinear seismic analysis of masonry buildings. *Eng Struct.* 2013;56:1787-1799.
8. Magenes G, Della Fontana AD. Simplified nonlinear seismic analysis of masonry buildings. *Proc Br Masonry Soc.* 1998;8:190-195.
9. AEDES. <https://www.aedes.it>
10. Penna A, Lagomarsino S, Galasco A. A nonlinear macroelement model for the seismic analysis of masonry buildings. *Earthquake Eng Struct Dynam.* 2014;43(2):159-179.
11. Vanin A, Foraboschi P. Modelling of masonry panels by truss analogy—part 1. *Masonry Int.* 2009;22(1):1.
12. Caliò I, Marletta M, Pantò B. A new discrete element model for the evaluation of the seismic behaviour of unreinforced masonry buildings. *Eng Struct.* 2012;40:327-338.

13. 3DMacro. <http://www.murature.com/3DMacro>
14. Marini A, Spacone E. Analysis of reinforced concrete elements including shear effects. *Struct J ACI*. 2006;103(5):646-655.
15. Raka E, Spacone E, Sepe V, Camata G. Advanced frame element for seismic analysis of masonry structures: model formulation and validation. *Earthquake Eng Struct Dynam*. 2015;44(14):2489-2506.
16. Mazzoni S, McKenna F, Fenves GL. OpenSees command language manual. Pacific Earthquake Engineering Research (PEER) Center; 2005.
17. Kent DC, Park R. Flexural members with confined concrete. *J Struct Div*. 1971;97(7):1969-1990.
18. Scott BD, Park R, Priestley MJN. Stress-strain behavior of concrete confined by overlapping hoops at low and high strain rates. *J Am Concr Inst*. 1982;79(1):13-27.
19. Mander JB, Priestley MJN, Park R. Theoretical stress-strain model for confined concrete. *J Struct Eng*. 1988;114(8):1804-1826.
20. FEMA 273. NEHRP Guidelines for the Seismic Rehabilitation of Buildings. Washington, DC: Building Seismic Safety Council; 1997.
21. Turnšek V, Čačovič F. Some experimental results on the strength of brick masonry walls. *Proceedings of the 2nd International Brick & Block Masonry Conference, Stoke-on-Trent, 1970*; 149–156.
22. Magenes G, Calvi GM. Cyclic behavior of brick masonry walls. *10th World Conference on Earthquake Engineering, Madrid, Spain, 1992*; 3:517–522.
23. Manzouri T, Shing PB, Amadei B, Schuller M, Atkinson R. *Repair and Retrofit of Unreinforced Masonry Walls: Experimental Evaluation and Finite Element Analysis*. Rep. No. CU/SR-95/2. Boulder, Colorado, USA: University of Colorado; 1995.
24. Anthoine A, Magonette G, Magenes G. Shear compression testing and analysis of brick masonry walls. *Proceedings of the 10th European Conference on Earthquake Engineering, Vienna, 1994*; 1657–1662.
25. Magenes G, Calvi GM, Kingsley GR. *Seismic Testing of a Full-Scale, Two-Story Masonry Building: Test Procedure and Measured Experimental Response, in Experimental and Numerical Investigation on a Brick Masonry Building Prototype—Numerical Prediction of the Experiment*. Report 3.0 G.N.D.T. Italy: University of Pavia; 1995.
26. Calvi GM, Kingsley GR, Magenes G. Testing of masonry structures for seismic assessment. *Earthq Spectra*. 1996;12(1):145-162.
27. Magenes G, Penna A, Senaldi I, Rota M, Galasco A. Shaking table test of a strengthened

full-scale stone masonry building with flexible

diaphragms. *Int J Archit Herit: Conservat Anal Restor.* 2014;8(3):349-375.

28. Senaldi I, Magenes G, Penna A, Galasco A, Rota M. The effect of stiffened floor and roof diaphragms on the experimental seismic

response of a full-scale unreinforced stone masonry building. *J Earthquake Eng.*

2014;18(3):407-443.

29. Senaldi I. *The Influence of Floor and Roof Diaphragms on the Seismic Response of Existing Masonry Buildings.* PhD Dissertation. Pavia:

ROSE School; 2012.

30. Dolce M. Schematizzazione e modellazione degli edifici in muratura soggetti ad azioni sismiche. *L'Industria Delle Costruzioni.*

1991;242:44-57. in Italian

31. Coleman J, Spacone E. Localization issues in force-based frame elements. *J Struct Eng.*

2001;127(11):1257-1265.

32. Binda, L., Tiraboschi, C., Roberti, G. M., Baronio, G., & Cardani, G. Experimental and numerical investigation on a brick masonry build-

ing prototype—Report 5.0—measuring masonry materials properties: detailed results from an extensive experimental research.

Politecnico di Milano, Dipartimento di Ingegneria Strutturale, 1995.

33. Magenes G, Penna A, Galasco A, Rota M. Experimental characterization of stone masonry mechanical properties. 8th International

Masonry Conference, Dresden, Germany, 2010; 247–256.

34. Magenes G, Galasco A, Penna A, Da Paré M. In-plane cyclic shear tests of undressed double leaf stone masonry panels. *Proc. 14th Euro-*

pean Conference on Earthquake Engineering, Ohrid, Macedonia, 2010; Paper No. 1435.

35. Beyer K. Peak and residual strengths of brick masonry spandrels. *Eng Struct.*

2012;41:533-547.

How to cite this article: Peruch M, Spacone E, Camata G. Nonlinear analysis of masonry structures using fiber-

section line elements. *Earthquake Engng Struct Dyn.* 2019;48:1345–1364.

<https://doi.org/10.1002/eqe.3188>